INSTITUTE OF PHYSICS PUBLISHING PLASMA PHYSICS AND CONTROLLED FUSION

Plasma Phys. Control. Fusion **45** (2003) 1143–1166 PII: S0741-3335(03)56683-0

Time-resolved two-dimensional plasma spectroscopy using coherence-imaging techniques

J Howard[1], **C Michael**[1], **F Glass**[1] **and A Danielsson**[2]

[1] Plasma Research Laboratory, Australian National University, Canberra ACT 0200, Australia
[2] Department of Electromagnetics, Chalmers University of Technology, SE-412 96, Göteborg, Sweden

Received 27 November 2002
Published 30 May 2003
Online at stacks.iop.org/PPCF/45/1143

Abstract

We describe methods for time-resolved imaging of the complex coherence of a spectral scene at one or more optical delays using electro-optically modulated polarization interferometers. By encoding the coherence information at harmonics of the electro-optic modulation frequency, it can be possible to obtain unambiguous spatio-temporal information about important physical parameters that govern the spectral content of the scene. We discuss the physical principles upon which the instrument is based and describe some applications in plasma spectroscopy, including Doppler tomography, Zeeman spectroscopy and relative line intensity measurements.

1. Introduction

It is well known that Fourier transform spectrometers (interferometers) offer some potential advantages over slit-coupled grating spectrometers, not least of which is the Jacquinot, or throughput advantage [1] and the ability to obtain two-dimensional spectral images. These advantages have not been previously exploited because of the perceived need to scan the interferometric optical path length delay in order to characterize the spectral coherence, and the difficulty of constructing stable optical interferometers with a wide field-of-view.

In the past few years we have been developing electro-optically modulated polarization interferometers for wide-field time-resolved 'coherence-imaging', with applications in plasma Doppler spectroscopy (including CXRS), polarization spectroscopy (Zeeman and MSE) and infrared thermography [2, 3]. When the spectral content of a scene can be successfully represented by a small number of free parameters (e.g. Doppler broadening, blackbody radiation, polarized multiplets), it is often the case that these parameters can be recovered from measurements of the complex coherence (phase and amplitude of the interferogram) at a small number of appropriately chosen fixed optical path length delays. After isolating the spectral feature of interest using an interference filter, we use one or more electro-optically modulated birefringent plates placed between a polarizer and analyser to encode the spectral information over a spread of harmonics of the modulation frequency. Using field-of-view widening

techniques, suitable imaging optics and two-dimensional detector arrays (fast-framing CCDs or multi-anode PMTs) it is possible to perform time-resolved two-dimensional spectral imaging.

In this paper, we report on recent technological advances and improvements in the performance of the modulated optical solid spectrometer (MOSS) coherence-imaging cameras. In particular, we discuss Doppler tomography of the ion velocity distribution function and report results obtained using single and multiple delay coherence-imaging cameras on the H-1 heliac at the ANU. As well, we show how the cameras can be used to image polarized multiplets and to interferometrically estimate spectral line intensity ratios.

2. Spectral line coherence

The Fourier transform spectrometer (interferometer) splits an incident scalar wave component $u(t)$, relatively delaying the nominally equal amplitude components by time τ before they are recombined at a square-law detector. In terms of the corresponding phase delay $\phi = 2\pi\nu\tau$, the intensity of the transmitted or reflected light at the final beam combiner, is proportional to

$$S_{\pm}(\phi) = \frac{I_0}{2}[1 \pm \Re[\tilde{\gamma}(\phi)]] \tag{1}$$

where $I_0 = \langle uu^* \rangle$ is the spectrally integrated irradiance, or brightness, and $\tilde{\gamma}$ is the complex coherence given by $\tilde{\gamma} = \langle u(t)u^*(t+\tau)\rangle / I_0$ where angle brackets denote a time average [4]. In general, the complex temporal coherence is related to the spectral distribution of the irradiance $I(\nu)$ through the Wiener–Khinchine theorem

$$\tilde{\gamma}(\phi) = \frac{1}{I_0}\int_{-\infty}^{\infty} I(\nu)\exp(\mathrm{i}2\pi\nu\tau)\,\mathrm{d}\nu. \tag{2}$$

For quasi-monochromatic radiation we can represent the field u as the analytic signal

$$u(t) = A(t)\exp(-\mathrm{i}2\pi\nu_0 t) \tag{3}$$

where the complex amplitude A changes slowly compared with the complex phasor [5]. The interferometric phase delay can also be approximated by

$$\begin{aligned}\phi &= 2\pi\nu\tau(\nu)\\ &\approx \phi_0 + \kappa\phi_0\xi\end{aligned} \tag{4}$$

where we have substituted $\nu = \nu_0(1+\xi)$ where $\xi = (\nu - \nu_0)/\nu_0$ is a normalized frequency difference coordinate, $\phi_0 = 2\pi\nu_0\tau_0$ where τ_0 is the centre-frequency time delay and where

$$\kappa = 1 + \frac{\nu_0}{\tau_0}\frac{\partial\tau}{\partial\nu}\bigg|_{\nu_0} \tag{5}$$

accounts for any optical frequency dispersion of the time delay. Using equation (4) in equations (1) and (2) obtains the quasi-monochromatic interferogram

$$S_{\pm}(\phi_0) = \frac{I_0}{2}[1 \pm \Re[\gamma(\hat{\phi}_0)\exp(\mathrm{i}\phi_0)]] \tag{6}$$

where the self coherence of the spectral line is given by

$$\gamma(\phi) = \frac{1}{I_0}\langle A(t)A^*(t+\tau)\rangle \tag{7}$$

$$= \frac{1}{I_0}\int_{-\infty}^{\infty} I(\xi)\exp(\mathrm{i}\phi\xi)\,\mathrm{d}\xi \tag{8}$$

and it is convenient to introduce the scaled phase delay coordinate

$$\hat{\phi}_0 = \kappa\phi_0. \tag{9}$$

To illustrate the properties of the interferogram, we consider the normalized spectral lineshape g characterized by spectral line shift $\xi_D = \nu_D/\nu_0$ and width $\sigma = \Delta\nu/\nu_0$

$$I(\nu) = I_0 g\left(\frac{\xi - \xi_D}{\sigma}\right). \tag{10}$$

The interferogram is obtained from equations (6) and (8) as

$$S = \frac{I_0}{2}[1 + \zeta\cos(\phi_0 + \phi_D)] \tag{11}$$

where, for a spectral profile having even symmetry, the fringe visibility, or contrast $\zeta \equiv |\gamma|$ and phase shift ϕ_D are given by

$$\zeta = G(\sigma\hat{\phi}_0) \tag{12}$$

$$\phi_D = \hat{\phi}_0\xi_D \tag{13}$$

where G is the Fourier transform of the lineshape g. Observe that variations in the line centre frequency ν_0 shift the interferogram phase but leave the fringe visibility ζ essentially unchanged. On the other hand, when the spectral width changes (but not the shift), only the fringe visibility is affected, the underlying phase remaining undisturbed. We show below that the decoupling of the shift and shape has important advantages for time-domain spectroscopic methods applied to Doppler tomography.

Measurements of the coherence at one or more fixed delay offsets ϕ_0 is sufficient to characterize a spectrum that can be described in terms of a small number of parameters. By using path-length modulation techniques to shift the coherence information to the temporal frequency domain, it is possible to perform two-dimensional time-resolved imaging of simple spectral scenes.

3. The MOSS spectrometer—instrument overview

The principal difficulty with the standard optical FTS is its sensitivity to mechanical and acoustic noise. The MOSS spectrometer is a polarization interferometer based on electro-optic and birefringent crystal plates (see figure 1). It is compact and has high optical throughput (compared with a grating spectrometer of comparable resolving power). By electro-optically modulating the optical path length, it is possible to image the interferogram contrast and phase at one or more fixed optical delays. For simple spectral scenes, the coherence information may be sufficient to recover the underlying physical quantities that influence the radiated spectrum.

Light is coupled to the MOSS system either directly or via lens-coupled optical fibres, before passing through a suitable filter (e.g. an optical interference filter) which isolates the spectral line or region of interest. The filtered beam is polarized before traversing a birefringent plate, such as lithium niobate, having its optic axis (or Z-axis) oriented at 45° to the plane of polarization. The birefringence gives rise to a fixed optial path length delay between the orthogonally polarized characteristic waves. Writing $k_0 = 2\pi\nu_0/c$, a plate of thickness L introduces a fixed phase delay $\phi \equiv \phi_0$ given by

$$\phi_0 = k_0 BL = 2\pi\nu_0\tau_0 \equiv 2\pi N \tag{14}$$

where N is the order of interference and $B = n_E - n_O$ is the birefringence of the delay plate and n_E and n_O are the extraordinary and ordinary wave refractive indices, respectively. The orthogonally polarized and relatively delayed waves that exit the birefringent delay plate are made to interfere by means of an analyser prior to detection. The resulting signal

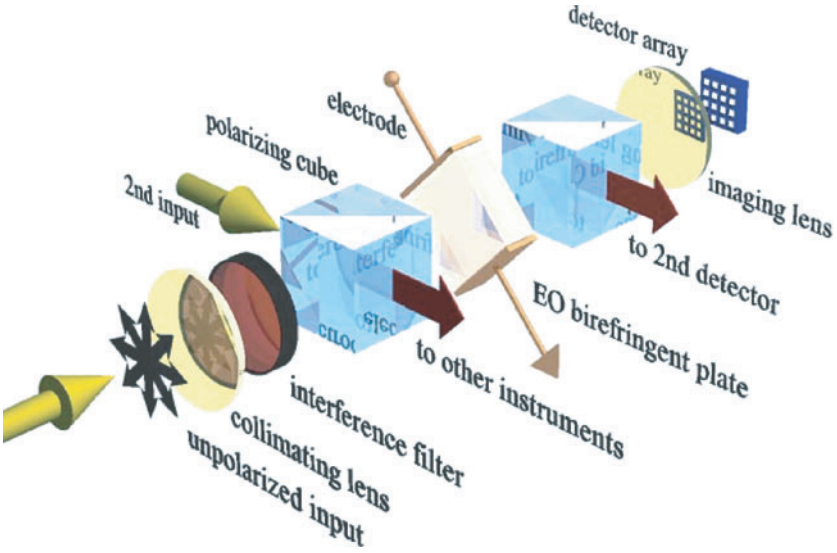

Figure 1. Optical layout for the modulated solid state spectrometer.

is given by equation (6) but with the incident brightness halved by the first polarizing beamsplitter.

The simplest way to measure the coherence at delay ϕ_0 is to sinusoidally modulate the optical path delay by $\phi_1 \gtrsim \pi/2$ so that the total time-varying interferometric phase is given by

$$\tilde{\phi}_0 = \phi_0 + \phi_1 \sin \Omega t. \tag{15}$$

Lithium niobate ($LiNbO_3$) is an artifical birefringent crystal ($n_E \sim 2.25$, $n_O \sim 2.35$) that also exhibits pyroelectric, piezoelectric, photoelastic, ferroelectric and electro-optic effects [6]. The delay modulation $\tilde{\phi}_1 = \phi_1 \sin \Omega t$ can be conveniently obtained by applying an oscillating electric field along the electro-optic crystal Z-axis transverse to the direction of the light propagation. The high voltage modulation of the electro-optic plate(s) is typically achieved using a function generator, a standard audio-amplifier and step-up transformer (100 : 1) to produce drive voltages of up to 4 kV p–p at frequencies in the range 1–50 kHz. The useful optical bandwidth of the system is set by the properties of the $LiNbO_3$ plate, which is transparent in the range 0.4–5 μm, though the use of BBO crystals could allow operation well into the ultraviolet (>190 nm).

When using phototube detectors, light signals are generally low pass filtered and amplified prior to synchronous data acquisition using $4f$, $8f$ or $16f$ synchronous external clocks, depending on the spread of harmonic carriers. When using integrating CCD detector arrays, the modulation is usually synchronized with the detector frame rate. Depending on the data rate, the signals can be demodulated in real time or analysed post-shot. Demodulation algorithms that self-consistently determine the modulation index ϕ_1 have been developed to suit staircase, sine wave and other modulation strategies.

3.1. Instrument response

We describe here only the most important features of the instrument function and performance. A detailed analysis is presented elsewhere [3].

For light collected from an extended source, the measured fringe visibility includes an instrumental component ζ_I such that $\zeta = \zeta_I \zeta_S$ where ζ_S is the lineshape-dependent fringe contrast at delay ϕ_0. The instrumental fringe contrast, which is analogous to the familiar slit function for grating spectrometers, is determined by the collected light solid angle and optical imperfections, and reduces the measurement sensitivity to variations in source contrast ζ_S. Dividing the measured fringe visibility by the known instrument contrast to obtain ζ_S is a much simpler process than the usual slit-function deconvolution correction required for grating based instruments.

The MOSS spectral resolution is proportional to the optical phase delay introduced by the birefringent plate. For example, a spectral line of width 0.1 nm and centred at 500 nm requires a plate producing a delay of roughly $\kappa N \sim 5000$ waves in order to be sensitive to changes in the optical coherence length. Note that it is necessary to account for the chromaticity of the birefringence which is given by the factor (see equation (5))

$$\kappa = 1 + \frac{\nu_0}{B_0}\frac{\partial B}{\partial \nu} \tag{16}$$

where $B_0 \equiv B(\nu_0)$. For $LiNbO_3$ at 488 nm, $\kappa = 1.54$ and is a slowly varying function of optical frequency. Given that the resolution of a grating spectrometer is inversely proportional to the entrance and exit slit widths, the MOSS light throughput advantage is most evident in high resolution applications. For interferometers, however, instrument contrast degradation with increasing collection solid angle can ultimately limit the useful light throughput at high resolution. It can be shown that the visibility decrement due to the integration over solid angle is negligible provided $\Omega \ll n^2/\kappa N$. This condition shows a trade-off between resolving power $\sim N$ and collection solid angle Ω, but is mitigated by a gain factor of $n^2/\sqrt{2}$, where n is the mean plate refractive index, compared with a free space Michelson interferometer [7].

It is a property of lithium niobate that the phase delay ϕ_0 drifts slowly in time due to ambient temperature variations. To overcome this problem it can be advantageous to separate the modulator and optical delay functions. Temperature-compensated lithium niobate modulators can be constructed by crossing two equi-thickness plates (to cancel the net birefringence) and reversing the polarities of the modulating voltage [8]. The loss of instrument contrast due to the static residual birefringence for off-axis rays can again be largely eliminated using field-widening techniques. Temperature-drift compensated compound delay plates can be constructed using birefringent crystals having different material properties [9].

3.2. Coherence-imaging cameras

We have constructed a number of one-dimensional and two-dimensional imaging systems for plasma cross-sectional imaging and tomography, and using both linear and two-dimensional multi-anode phototube arrays and fast-framing CCD arrays [10, 9]. The cameras uses standard photographic lenses and 50 mm optics with typically ~40 mm clear aperture to match that of the birefringent plates. The cameras are modular in construction, using interchangeable flanged components that can be bolted to an optical rail.

Because rays from different plasma spatial positions are angularly multiplexed through the MOSS optical components, a key issue is the degradation of the instrument contrast associated with the angular variation of the phase delay introduced by the birefringent plate. In imaging applications using polarization interferometers, a wide field-of-view can be achieved by using crossed birefringent crystals with an intervening half wave plate at an azimuth of 45° [7,10]. The resulting field-of-view is expanded by a factor $[2\sqrt{2}n/B]^{1/2} \sim 8$ to typically tens of degrees or more. The instrument response can be measured by illuminating the field of view with a

suitably diffused monochromatic light source (in our case, laser beam) having wavelength at or near the wavelength of interest.

4. Doppler spectroscopy and tomography

Doppler spectroscopy is a routine diagnostic for sensing the gross features of the velocity distribution of excited species in radiating, optically thin media such as plasmas [11, 12]. Despite the simple linear mapping from velocity distribution to emission spectrum via $\xi \equiv V/c$, interpretation is complicated by the fact that the Doppler shift conveys only the velocity component in the direction of view. For example, for a uniform medium in thermal equilibrium, and provided other line broadening mechanisms can be ignored, the spectral lineshape is a Gaussian whose width and shift are related respectively to the temperature and to the component of the gross motion (e.g. rotation) of the emitting species in the direction of view. When the distribution function is inhomogeneous, the measured spectrum is the local brightness-weighted summation of Gaussians of varying width and shift. The problem thus combines the three-dimensional Radon transform of the velocity distribution function (integration over planes) brought about by the Doppler effect and the two-dimensional Radon transform (integration over lines) of the spatially inhomogeneous radiating source. Even with complete measurements (i.e. line-integrated measurements at all angles and impact parameters), the general inverse Doppler tomography problem is singular.

It has been shown recently that for the case of drifting local thermal equilibrium, tomographic measurements of the light coherence at a single fixed delay suffice for the reconstruction of the emissivity (dc), flow vorticity (phase) and species temperature (fringe visibility) [13]. Measurements of the coherence at a number of distinct delays provide additonal independent constraints that ensure good condition for the inverse problem or enable the reconstruction of distribution functions that are isotropic in the drifting frame.

We consider spectral line radiation (centre frequency ν_0) from an extended, isotropically radiating and optically thin inhomogeneous plasma. For simplicity, we approximate the measurement as a simple line integral of the emission along the line $L(p, \theta)$ with impact parameter p and angle θ (direction $\hat{\boldsymbol{p}} = (\cos\theta, \sin\theta)$ orthogonal to $\hat{\boldsymbol{l}}$) in the observation cross-section (see figure 2). The measured emission spectrum $e(\xi; \hat{\boldsymbol{l}})$ can then be written as an integral of the local brightness-weighted spectral irradiance $g(\boldsymbol{r}, \xi; \hat{\boldsymbol{l}})$ where $\boldsymbol{r}$ is a position

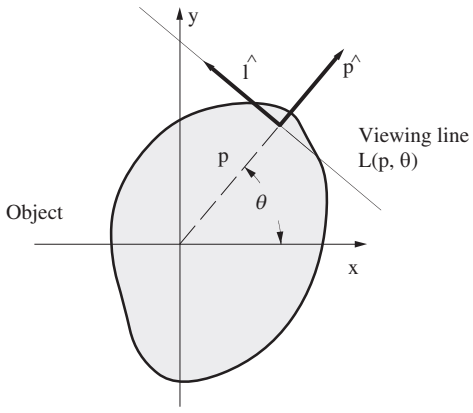

Figure 2. Geometry for the optical tomography problem.

vector in the medium:

$$e(\xi;\hat{\boldsymbol{l}}) = \int I_0(\boldsymbol{r})g(\boldsymbol{r},\xi;\hat{\boldsymbol{l}})\delta(p-\boldsymbol{r}\cdot\hat{\boldsymbol{p}})\,\mathrm{d}\boldsymbol{r}$$
$$\equiv \int_L I_0(\boldsymbol{r})g(\boldsymbol{r},\xi;\hat{\boldsymbol{l}})\,\mathrm{d}l. \tag{17}$$

Assuming the Doppler effect is the predominant line-broadening mechanism, the local spectral irradiance is proportional to

$$g(\boldsymbol{r},\xi;\hat{\boldsymbol{l}}) = \int f(\boldsymbol{r},\boldsymbol{v})\delta(\xi-\boldsymbol{v}\cdot\hat{\boldsymbol{l}})\,\mathrm{d}\boldsymbol{v}. \tag{18}$$

The delta function selects those particles in the normalized velocity distribution of the radiating species $f(\boldsymbol{r},\boldsymbol{v})$, where $\boldsymbol{v}=\boldsymbol{V}/c$ and $\boldsymbol{V}$ is the species velocity vector, having component $\boldsymbol{v}\cdot\hat{\boldsymbol{l}}$ giving rise to normalized frequency shift ξ. When the radiating medium is in drifting LTE, the distribution function in the frame drifting locally with velocity $\boldsymbol{v}_D(\boldsymbol{r})$ is given by

$$f_0(\boldsymbol{r},v) = (\pi v_{\mathrm{th}}^2)^{-3/2}\exp\left(-\frac{v^2}{v_{\mathrm{th}}^2}\right) \tag{19}$$

where $v_{\mathrm{th}}(\boldsymbol{r})$ is the thermal velocity. The local emission spectrum in the direction $\hat{\boldsymbol{l}}$ is obtained on substitution into equation (18) as

$$g(\boldsymbol{r},\xi) = (\pi\xi_{\mathrm{th}}^2)^{-1/2}\exp\left[-\frac{(\xi-\boldsymbol{v}_D\cdot\hat{\boldsymbol{l}})^2}{\xi_{\mathrm{th}}^2}\right] \equiv g_0(\boldsymbol{r},\xi-\boldsymbol{v}_D\cdot\hat{\boldsymbol{l}}) \tag{20}$$

where $\xi_{\mathrm{th}} \equiv v_{\mathrm{th}}(\boldsymbol{r})$ is the Doppler thermal width. Since the exponent involves $\boldsymbol{r}$-dependent unknowns $\boldsymbol{v}_D\cdot\hat{\boldsymbol{l}}$ and ξ_{th}, and because the frequency-domain measurement convolves $g(\boldsymbol{r},\xi)$ with the instrument spectral response, the tomography of the spectral irradiance $e(\xi;\hat{\boldsymbol{l}})$ presents a difficult inverse problem (see equation (17)).

By contrast, the local spectral coherence, which is the Fourier transform of the local spectrum, assumes a particularly simple separable form

$$G(\boldsymbol{r},\hat{\phi}_0) = \exp(\mathrm{i}\hat{\phi}_0\boldsymbol{v}_D\cdot\hat{\boldsymbol{l}})G_0(\boldsymbol{r},\hat{\phi}_0). \tag{21}$$

Here, G_0, which is the Fourier transform of the lineshape in the locally drifting frame, is given by

$$G_0(\boldsymbol{r},\hat{\phi}_0) = \exp\left(-\frac{\hat{\phi}_0^2\xi_{\mathrm{th}}^2}{4}\right)$$
$$\equiv \exp\left[-\frac{T_S(\boldsymbol{r})}{T_C}\right] \tag{22}$$

where $T_S(\boldsymbol{r})$ is the local species temperature and T_C is the instrument 'characteristic temperature'

$$kT_C = \tfrac{1}{2}m_S V_C^2 \qquad V_C = \frac{2c}{\hat{\phi}_0}. \tag{23}$$

For optimum sensitivity to temperature changes, the characteristic temperature is chosen to be close to the expected source temperature requiring $\hat{\phi}_0 v_{\mathrm{th}} = 2$.

Measurement of the coherence γ of the emission spectrum $e(\xi;\hat{\boldsymbol{l}})$ at some fixed phase delay ϕ_0 delivers the fringe contrast

$$|\gamma(\hat{\phi}_0;\hat{\boldsymbol{l}})| = \frac{1}{e_0}\int_L I_0(\boldsymbol{r})\exp\left[-\frac{T_S(\boldsymbol{r})}{T_C}\right]\mathrm{d}l \tag{24}$$

where

$$e_0 = \int_L I_0(\boldsymbol{r})\,\mathrm{d}l \tag{25}$$

is the line-integrated brightness. Provided that $\hat{\phi}_0 \boldsymbol{v}_D \ll 1$, a quantity related to the species flow velocity can be obtained from the interferometric phase shift

$$\phi_D = \frac{\hat{\phi}_0}{e_0|\gamma|} \int_L I_0(\boldsymbol{r})\,\exp\left[-T_S(\boldsymbol{r})/T_C\right] \boldsymbol{v}_D \cdot \mathrm{d}l. \tag{26}$$

The phase offset $\hat{\phi}_0$ can be chosen to magnify the usually small Doppler shift component but not so large as to invalidate the first order approximation leading to equation (26). It is apparent that the signals from a modulated, single fixed delay FTS can be related directly to line integral measurements of the scalar field $I_0 G_0$ and longitudinal line integral measurements of the vector field $I_0 G_0 \boldsymbol{v}_D$.

4.1. MOSS camera Doppler measurements in the H-1 heliac

The MOSS camera is mounted in front of a vacuum tank port and views the plasma via a pair of elongated flat mirrors that are supported inside the vacuum tank. The viewing geometry for the camera is shown in figure 3. The full angle subtended by the plasma at the detector plane is $\sim 6.5^\circ$ while the imaging system magnification can be set between 10X and 15X. The plasma poloidal cross-section is imaged through the MOSS optics onto 16 or 32 channel multi-anode phototube arrays.

Combined with information from the scanning far-infrared interferometer [14], and single channel MOSS systems viewing toroidally, the camera has been used to study the dynamical radial force balance during confinement transitions in rf-sustained (7 MHz, 80 kW) discharges in argon at low magnetic field strengths (0.1 T) in the H-1 heliac. The H-1 heliac is a helical-axis toroidal magnetic plasma confinement device having major radius $R = 1$ m and a bean-shaped plasma cross-section of average minor radius $a \sim 0.2$ m. The ion temperatures for these discharges, measured from the Doppler broadening of the Ar II $^2D_{5/2} \rightarrow {}^2P_{3/2}$ transition at 488 nm, range between 5 and 20 eV, increasing with magnetic field strength and decreasing with neutral fill pressure. Raw projection data for a low-field (0.06 T) discharge exhibiting a spontaneous transition to improved confinement are presented in figure 4. At the transition

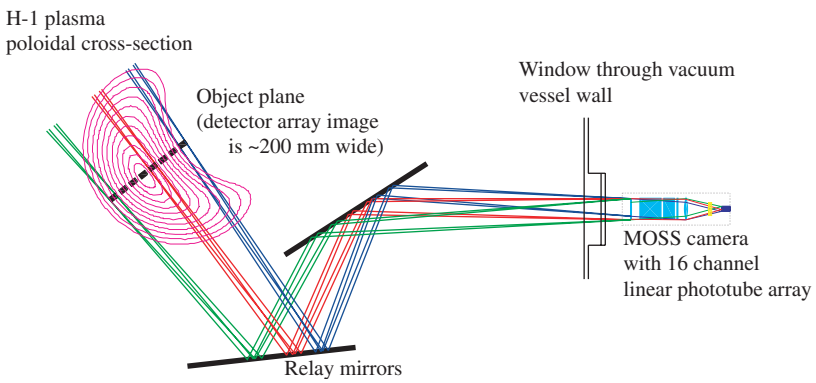

Figure 3. Diagram showing the plasma region viewed by the H-1 MOSS camera. Mirrors internal to the vacuum vessel direct the plasma emission from a poloidal cross-section to the camera. The central and extreme viewing chords are shown.

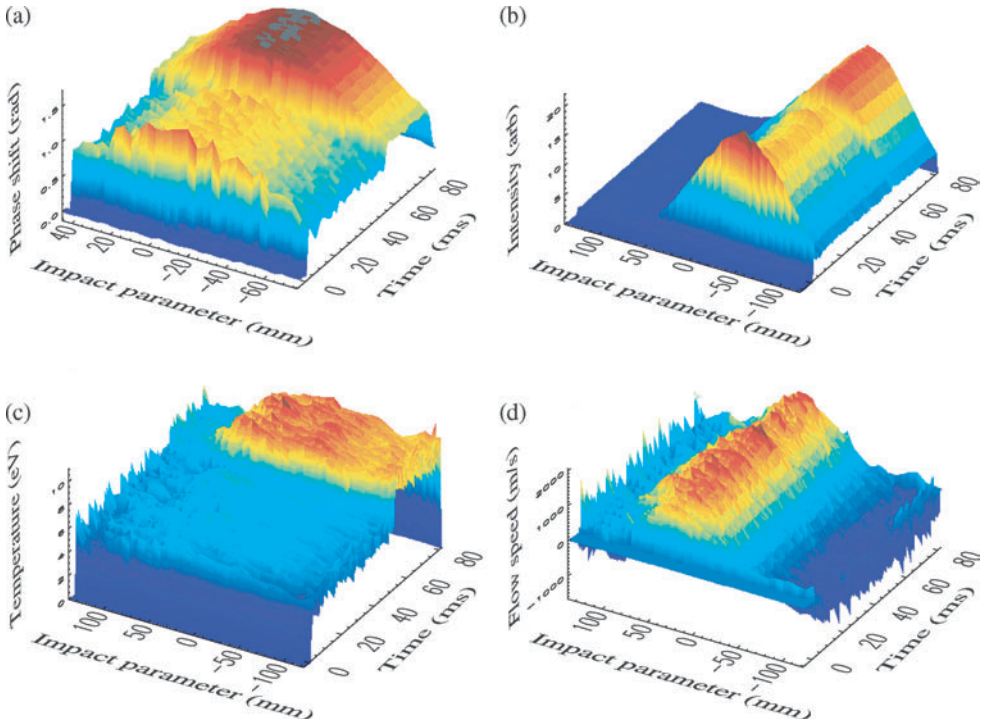

Figure 4. Temporal evolution of (*a*) scanning interferometer density projection, and MOSS camera poloidal projections of (*b*) brightness, (*c*) ion tempeature and (*d*) flow speed (bottom) for an argon discharge at 0.06 T showing a transition from poor to improved confinement. At the transition the ion temperature increases from 6 to 9 eV within 1 ms while there is little change to the plasma flow speed.

the temperature increases by 30% to 9 eV and the density profile becomes more peaked. There is little change in the plasma flow speed. The results of tomographic unfolding of the projections (assuming that plasma conditions are constant on a flux surface) will be presented elsewhere [15].

For conditions of higher field strength or lower neutral fill pressure, we have observed inconsistencies in the force balance-inferred radial electric field using measurements at different crystal plate delays. There is also evidence for significant anisotropy of the distribution function. Closer study has revealed a substantial cold ion component (evident across the projection), possibly due to charge exchange with the background neutrals. The measured coherence as a function of delay plate thickness at the central probing chord and (25 mm thickness of $LiNbO_3$ is equivalent to $\hat{\phi}_0/2\pi = 7300$ waves at 488 nm) for plasma discharges at 0.06 and 0.12 T is shown in figure 5. The coherence at 0.12 T shows a clear departure from Gaussian, and is well fitted by a two-component model with temperatures 30 eV (0.6 fraction) and 3 eV (0.4 fraction). The large cold fraction may be due to the relatively poor confinement of hot argon ions in these low-field ($r_L/a \sim 0.3$) discharges. Additional broadening mechanisms such as Zeeman effect can be neglected under these discharge conditions. Confirming these findings, figure 6 shows the plasma-pulse-integrated spectral profile for the 488 nm line measured using a high resolution grating spectrometer and CCD array. The dotted curve is the computed lineshape based on the coherence measurements and the solid curve which fits the measurements is the convolution of the two-temperature profile with the measured

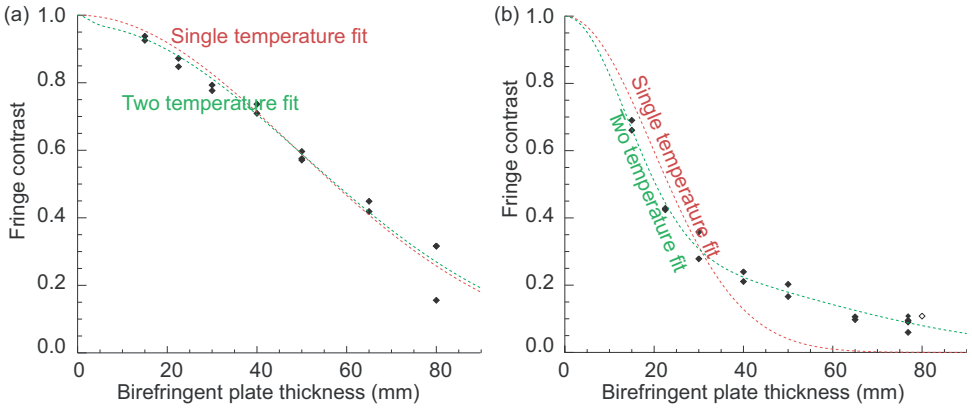

Figure 5. Measurements of contrast degradation versus birefringent delay under different plasma discharge conditions (*a*) 0.06 T and (*b*) 0.12 T. A simple interpretation of the contrast degradation in terms of species temperature is not always justified.

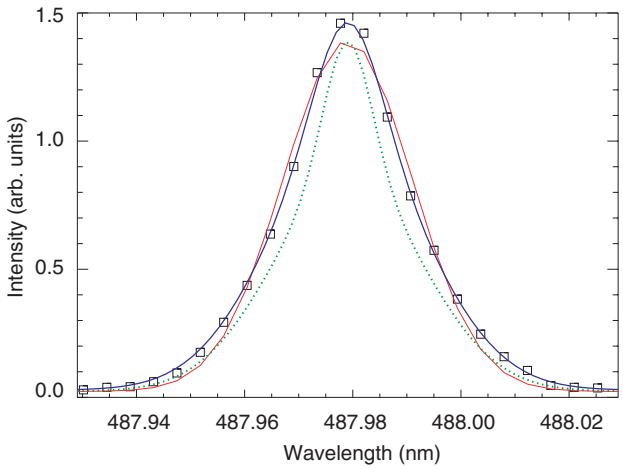

Figure 6. The computed spectral lineshape based on the two temperature fit to the data of figure 5 is shown as the dotted curve. The two temperatures are 30 and 3 eV with a 40% cold fraction. The symbols show the spectrum measured using a high resolution grating spectrometer and CCD array, while the solid curve conforming closely with the symbols is the result of convolving the two-temperature lineshape with the measured slit function. The remaining broad curve is the best-fit Gaussian which indicates a 'temperature' of 22 eV.

spectrometer slit function. The agreement is excellent. Because the strongly non-Gaussian distortion of the coherence profile is more or less apparent along all viewing chords, it is unlikely due to any strong inhomogeneity of the plasma temperature distribution. The results indicate the need for simultaneous measurements at a number of delays for the characterization of such non-thermal distributions. We return to this issue in section 7.

5. Spectroscopy of polarized multiplets

It is well known that spectral lines can be split, shifted and polarized by magnetic and electric fields (the Zeeman and Stark effects, respectively). The magnitude of the splitting and the

polarization orientation of the multiplet components convey information about the vector fields. Modulating the polarization state of the multiplet varies the spectral content of the light. The change in the spectral shift or width can be then sensed by the MOSS spectrometer as a change in the interferogram phase or contrast. The phase and amplitude of these modulations give information about the orientation and magnitude of the originating field. The suitability of such techniques for measurement of motional Stark effect emission from injected neutral beams is discussed in [16]. Here, we briefly review the Zeeman effect and present experimental results illustrating the utility of coherence-based techniques.

5.1. Zeeman effect

The measurement of the poloidal magnetic field in a tokamak from the Zeeman splitting and polarization of the magnetic dipole radiation from heavy ions was suggested by Feldman [17]. While first results were promising [18], the low light flux precluded time-resolved measurements. Accurate measurements of the poloidal field profile in the outer region of JIPP T-IIU discharges during current ramping experiments have been obtained by measuring the Zeeman splitting of He II (468.8 nm) using a Fabry–Perot interferometer [19]. Measurement of the emission from an injected lithium beam has also been recently proposed for edge current density measurements on DIII-D [20].

The upper and lower electronic levels of an atom or ion in a weak magnetic field are split into $2J + 1$ sublevels with energy shifts given by

$$\Delta E_{JM} = g_{\alpha JM} M \mu B \tag{27}$$

where, for L–S coupling, $g_{\alpha JM}$ is the Landé splitting factor, μ is the Bohr magneton and α denotes quantum numbers other than the total angular momentum J and magnetic quantum number M, where $|M| \leqslant J$. Because of these shifts, the spectral line is split into a number of components whose relative intensities and polarizations depend on the corresponding changes in J and M [17, 21]. Viewed along $\boldsymbol{B}$, the emission is zero for the $\Delta M = 0$ lines and is circularly polarized clockwise for $\Delta M = +1$ and counterclockwise for $\Delta M = -1$. Viewed in the direction perpendicular to $\boldsymbol{B}$, the emission is linearly polarized perpendicular to $\boldsymbol{B}$ for $\Delta M = \pm 1$ and parallel to $\boldsymbol{B}$ for $\Delta M = 0$. For high temperature plasmas, this splitting is usually small compared to the Doppler broadening, so that polarization tagging of the frequency shifted Zeeman components is essential for their discrimination against the unshifted component.

To describe the polarization state, we take a coordinate system where γ is the angle between the magnetic field and the line-of-sight (taken to be in the z direction) and β is the angle between the projection of $\boldsymbol{B}$ onto the orthogonal x–y plane and the x axis (figure 7). The spectrum and polarization state of the emission is the line-of-sight integral of the contributions from all components of the Zeeman multiplet. With appropriate processing of the polarization state, the first spectral moment of the multiplet (obtained from the interferometric phase) can be shown to be proportional to the brightness-weighted component of the magnetic field along the viewing line-of-sight [22].

Using a polarimeter to transmit alternately the π and σ manifolds, results in a modulation of the spectral width of the multiplet. By combining the polarimeter with a MOSS spectrometer of appropriate delay offset, it is possible to detect the associated changes in fringe contrast. The phase of the contrast modulation (relative to the polarimeter modulator phase) gives the magnetic field azimuth β, while the modulation depth is related to the magnetic field strength. The polarimeter can also be configured to switch between the left and right hand circular polarization components that are visible when the projection of the magnetic field line onto the line-of-sight is non-zero ($\gamma \neq \pi/2$). This switching modulates the first spectral moment and leads to a modulation in the interferometric phase.

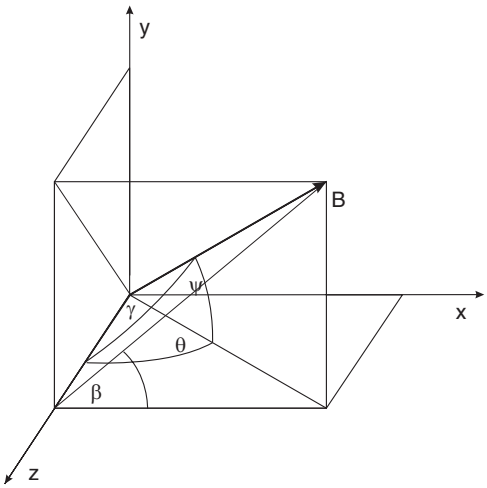

Figure 7. Geometry for analysis of Zeeman effect. The viewing line is along the x-axis.

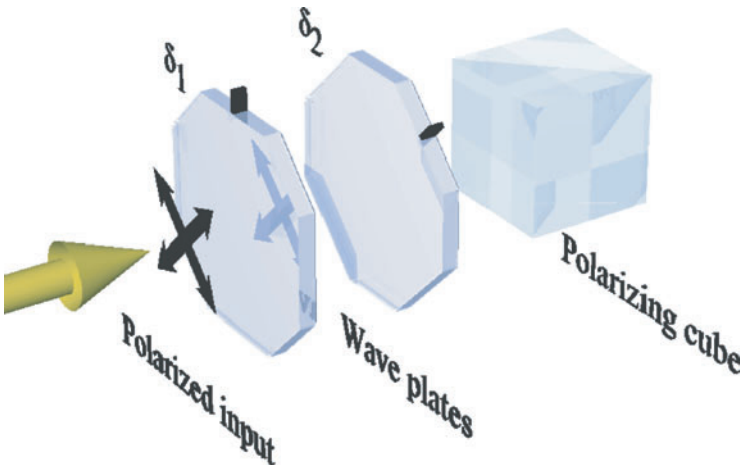

Figure 8. Layout for the spherical quadrature polarimeter. The birefringent waveplates are mutually oriented at 45° and introduce delays δ_1 and δ_2.

We have constructed a polarimeter (figure 8) capable of isolating any or all of the Stokes parameters that characterize the light polarization state [16]. The polarimeter uses two birefringent phase plates (delays δ_1 and δ_2) having their fast axes mutually oriented at 45°. The plates are followed by an analyser oriented to transmit light which is polarized perpendicular to the fast axis of the first phase plate (i.e. polarized along the x direction in figure 7). We represent the incident polarized electric field as the complex vector

$$\boldsymbol{E} = \begin{pmatrix} \cos\chi \exp(-j\varphi) \\ \sin\chi \end{pmatrix} \tag{28}$$

where $\tan\chi = |E_y|/|E_x|$ and φ is the phase angle between the x and y components of the wave and the time dependence is ignored. The intensity of the light transmitted by the final

analyser is given by

$$P = \frac{I_0}{2}(1 + \boldsymbol{s} \cdot \boldsymbol{p}) \tag{29}$$

$$\boldsymbol{s} = (\cos 2\chi, \sin 2\chi \cos\varphi, \sin 2\chi \sin\varphi) \tag{30}$$

$$\boldsymbol{p} = (\cos\delta_2, \sin\delta_2 \cos\delta_1, \sin\delta_2 \sin\delta_1). \tag{31}$$

Observe that equation (31) defines an optical phase shift vector analogous to the Stokes vector.

The polarization state of the Zeeman emission components depends on angles (γ, β) defining the orientation of the magnetic field. This relationship can be conveniently expressed using the Stokes vectors for the central and shifted spectral components (see appendix)

$$\boldsymbol{s}_\pi = \frac{1}{\sin^2\gamma}(s_1, s_2, 0) \tag{32}$$

$$\boldsymbol{s}_{\pm\sigma} = \frac{1}{1 + \cos^2\gamma}(-s_1, -s_2, \mp s_3) \tag{33}$$

where

$$(s_1, s_2, s_3) \equiv (\sin^2\gamma \cos 2\beta, \sin^2\gamma \sin 2\beta, 2\cos\gamma) \tag{34}$$

and $|\boldsymbol{s}_\pi| = |\boldsymbol{s}_{\pm\sigma}| = 1$. The intensities for the components vary with polar angle according to

$$I_\pi(\gamma) = \frac{I_0}{2}\sin^2\gamma \tag{35}$$

$$I_{\pm\sigma}(\gamma) = \frac{I_0}{4}(1 + \cos^2\gamma) \tag{36}$$

where I_0 is the spectrally integrated irradiance, or brightness of the multiplet. Because the total spectrally integrated multiplet emission is unpolarized, the π and σ components need to be isolated from one another in order that the polarization analysis can reveal directional information about the magnetic field.

5.2. Coherence of the Zeeman multiplet

An equivalent approach to spectral discrimination, is to exploit the difference in the coherence of the π and σ manifolds by combining the polarimeter with a coherence imaging system. In combining the systems, the final polarimeter analyser also serves as the first polarizing element of the MOSS camera. The resulting optical layout is shown in figure 9.

The signal S obtained from the polarimeter-MOSS system is given by

$$\frac{4S}{I_0} = I_\pi(1 + \boldsymbol{s}_\pi \cdot \boldsymbol{p})(1 + \zeta_\pi \cos\tilde{\phi}_0) + I_{\sigma_+}(1 + \boldsymbol{s}_{\sigma_+} \cdot \boldsymbol{p})[1 + \zeta_{\sigma_+}\cos(\tilde{\phi}_0 + \Delta)] + I_{\sigma_-}(1 + \boldsymbol{s}_{\sigma_-} \cdot \boldsymbol{p})[1 + \zeta_{\sigma_-}\cos(\tilde{\phi}_0 - \Delta)] \tag{37}$$

where $\tilde{\phi}_0$ is the modulation phase (equation (15)), ζ_π and $\zeta_{\sigma\pm}$ are the component contrasts at scaled delay $\hat{\phi}_0 = \kappa\phi_0$ and Δ is the phase shift associated with the intensity-weighted centre-of-mass shift of the σ components from ξ_0. We assume for simplicity a normal Zeeman triplet with components sharing a common spectral lineshape $g(\xi)$ that is determined by effects such as Doppler broadening (i.e. $\zeta_\pi = \zeta_{\sigma\pm} \equiv \zeta$). The magnetic-field dependent phase shift is then given by

$$\Delta = \hat{\phi}_0 \xi_B \equiv \hat{\phi}_0 \frac{g_{\alpha J M}}{2}\frac{\nu_c}{\nu_0} \tag{38}$$

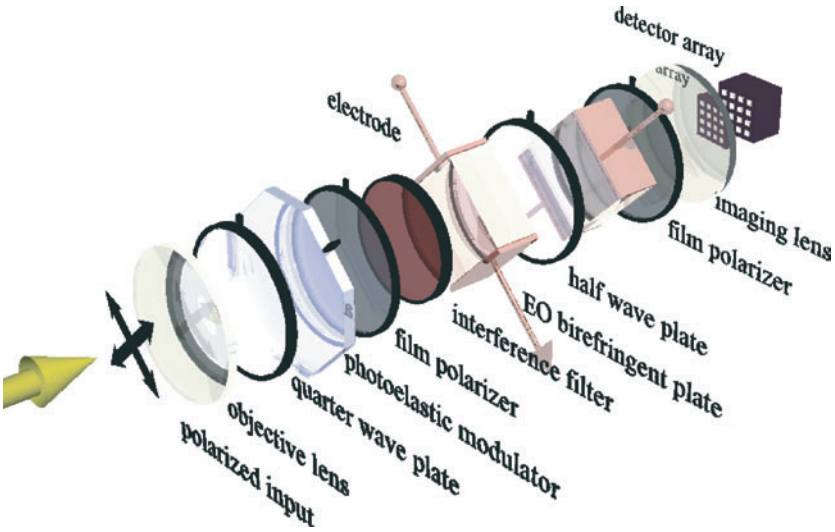

Figure 9. Layout for the combined spherical quadrature polarimeter/MOSS spectrometer. In this depiction, the electro-optic modulator/delay plate is field widened, and the polarimetric modulation is effected using a photoelastic modulator. The polarimeter x-axis is indicated by the tag on the film polarizers.

where $\nu_c = eB/2\pi m_e$ is the cyclotron frequency. With some straightforward algebra, equation (37) reduces to

$$\frac{4S}{I_0} = 1 + \zeta \cos^2\left(\frac{\Delta}{2}\right)\left\{\cos\tilde{\phi}_0\left[1 - \cos^2\gamma\tan^2\left(\frac{\Delta}{2}\right) + (s_1p_1 + s_2p_2)\tan^2\left(\frac{\Delta}{2}\right)\right]\right.$$
$$\left. + \sin\tilde{\phi}_0 s_3 p_3 \tan\left(\frac{\Delta}{2}\right)\right\}. \tag{39}$$

The terms independent of the Stokes parameters account for the contrast change associated with the orientation-dependent relative intensity of the shifted and unshifted components. In the absence of the polarimeter (i.e. $\delta_1 = \delta_2 = 0, \boldsymbol{p} = (1, 0, 0)$), the received signal reduces to equation (11) with fringe contrast

$$\zeta_B = \zeta_\sigma + (\zeta_\pi - \zeta_\sigma)\sin^2\gamma\cos(2\beta) \tag{40}$$

where we have set $\zeta_\pi \equiv \zeta$ and denoted $\zeta_\sigma \equiv \zeta\cos\Delta$ as the effective contrast of the σ pair of lines. When viewing along $\boldsymbol{B}$, $\gamma = 0$ and the contrast is sensitive only to the two circular σ components. When viewing transverse to $\boldsymbol{B}$ the fringe contrast depends on the mixture of components transmitted by the first polarizing plate. For example, when $\beta = 0$, only the π component is analysed by the MOSS spectrometer and $\zeta = \zeta_\pi$.

In total, there are four unknown quantities, the Zeeman component contrast ζ, the magnetic field strength Δ and the orientation angles γ and β. There are a number of possible strategies for extraction of these parameters. For example, setting $\delta_1 = \delta_2 = (\pi/2)\sin(\Omega_P t)$ generates a spread of harmonic carriers that encode the field strength as well as combinations of the orientation angles (γ, β) (we assume Ω_P is significantly less than the MOSS modulation frequency Ω). We here consider some simple cases that illustrate the instrument behaviour.

Upon inspection of equation (39) it is apparent that by setting $\delta_1 = 0$ and modulating $\delta_2 \equiv \delta_2\sin(\Omega_P t)$ it is possible to probe the magnetic field azimuth β. If the delay amplitude is π radians, this is equivalent to placing a switching half wave plate in front of the MOSS

spectrometer that alternately selects the π (narrowband) and σ (broadband) components. In this case, the final interferogram now has fringe contrast

$$\zeta_B = \zeta_\sigma + (\zeta_\pi - \zeta_\sigma)\sin^2\gamma\cos^2\left(\frac{\delta_2}{2} - \beta\right) \tag{41}$$

consisting of a dc component $\zeta_{\rm dc} \equiv \zeta_\sigma = \zeta\cos\Delta$ and a modulation of amplitude $\zeta_{\rm ac} \equiv (\zeta_\pi - \zeta_\sigma)\sin^2\gamma$ and phase (relative to the polarimeter angle δ_2) given by the azimuthal angle β. The modulation amplitude, which depends on the component separation induced by the magnetic field, can be optimized with appropriate choice of the phase delay introduced by the birefringent plate. The ability to discern the modulation induced by the magnetic field when thermal broadening is significant is considered in section 6.1. Note that when the line-of-sight is aligned with the magnetic field ($\gamma = 0$), the π component is no longer visible, and the modulation disappears.

Equation (39) also shows that the interferometric phase is sensitive to variations in the polar tilt angle γ through the term $s_3 p_3$. If we set $\delta_1 = \delta_2 = \pi/2$ [$\boldsymbol{p} = (0, 0, 1)$], the interferometric phase shift generated by the spectral separation of the orthogonal elliptically polarized σ components is given by

$$\tan\left(\frac{\phi_B}{2}\right) = \cos\gamma\tan\left(\frac{\Delta}{2}\right). \tag{42}$$

When $\gamma = 0$ (viewing along B), the phase excursion $\phi_B = \Delta$ corresponds to the spectral shift of the σ_+ component. When the phase of δ_2 reverses, the σ_- component is detected and the phase shift ϕ_B also reverses. Determination of γ from knowledge of ϕ_B, however, also requires knowledge of the magnetic field strength. From the foregoing, it is clear that only β can be recovered directly. However, using some basic trigonometry, the measured quantities can be combined to give the component contrast ζ:

$$\zeta = \frac{\zeta_{\rm dc} + \zeta_{\rm ac}\cos^2(\phi_B/2)}{\cos\phi_B}. \tag{43}$$

With knowledge of ζ, the other quantities follow directly.

Given the wide field of view, a polarimeter/MOSS camera can be located close to a plasma viewing port and the interferograms relayed by optical fibre to one or more detector arrays. Since the full multiplet is observed, only a relatively wideband interference filter is required to isolate the spectrum. Finally, because the polar and azimuthal angles (γ, β) are carried by the modulation components, some information can be obtained without concern for instrument calibration or possible pollution of the passband by unpolarized background.

5.3. Measurements on a magnetized lamp

To test the system performance we have measured the Zeeman splitting of the $^3S_1$–$^3P_0$ transition at 468 nm ($\kappa = 1.60$) in a zinc dc discharge lamp (18 V, 2 A) placed between the poles of a Helmholtz coil electromagnet. Observing in a direction perpendicular to the magnetic field $\gamma = \pi/2$, and choosing $\delta_1 = 0$ and $\delta_2 = \pi$ (half wave plate) the first MOSS polarizer transmits only the two outer σ components of the normal triplet ($\beta = \pi/2$). The detector then senses the superposition of the separate interferograms:

$$S = \frac{I_0}{4}[1 + \zeta\cos\Delta\cos\tilde{\phi}_0]. \tag{44}$$

The beating of the two interferograms gives rise to a B-dependent cosinusoidal modulation of the fringe contrast that can be measured by electro-optically modulating the MOSS phase delay as usual.

We have ramped the magnetic field and recorded the demodulated MOSS interferogram. The magnetic field strength is monitored using a Hall probe whose calibration was checked against standard magnets and confirmed by measurements of the Zeeman splitting using a high-resolution grating spectrometer. Figure 10 shows the recorded fringe contrast versus magnetic field strength obtained using a 4-crystal MOSS system of total thickness $L = 100\,\mathrm{mm}$. Superimposed is the expected contrast modulation. The close agreement confirms the result for the wavelength-dependent delay dispersion given by equation (4).

If the field is not normal to the line-of-sight, the σ components become elliptical. An initial quarter wave plate $\delta_1 = \pi/2$ converts the circular components to linear. Subsequent modulation of δ_2 then shifts the interferometer phase as the mixture of σ_+ and σ_- components transmitted by the polarizer is varied. The effect is shown in figure 11 for magnetic field

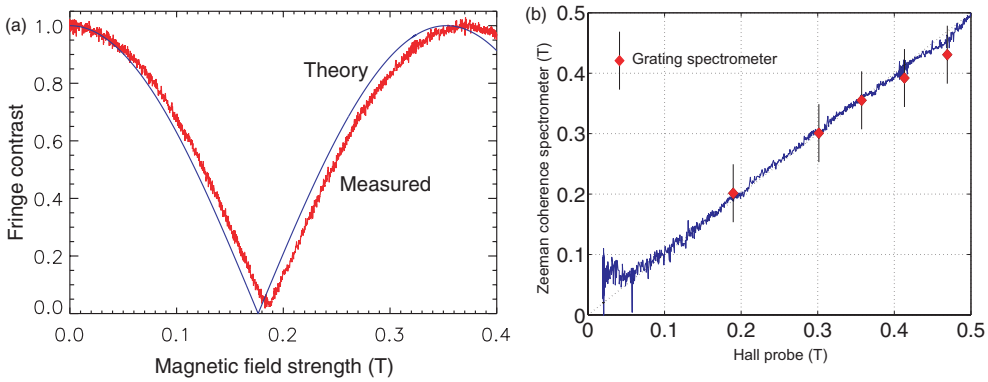

Figure 10. (*a*) The measured and calculated variation of fringe contrast with magnetic field strength for the σ components of the Zn 468 nm emission line. The discrepancy between the theoretical and measured beat patterns may be attributed to remnant unaccounted magnetization of the electromagnet pole pieces. (*b*) The inferred magnetic field strength versus Hall probe estimate. For comparison, estimates of the field strength obtained using a high resolution grating spectrometer measuring the splitting of the σ components of the Zeeman multiplet are overlaid.

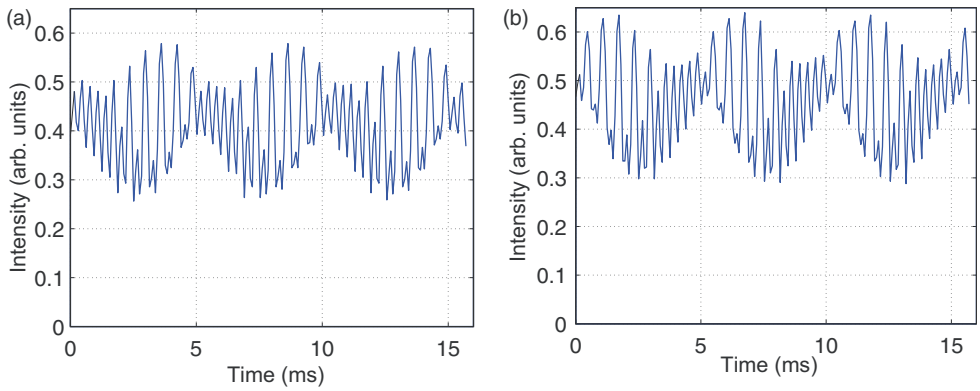

Figure 11. (*a*) Zeeman MOSS spectrometer signal when viewing the magnetic field at angle $\gamma = 105^\circ$ and (*b*) $\gamma = 75^\circ$. Because the radiation is elliptically polarized, the interferogram phase is modulated by the spectral shifting introduced by the sinusoidally varying phase delay δ_2 applied to the second polarimeter wave plate. The spectral shifting introduced by the polarimeter modulation (slow component) changes the ratio of the fundamental and second harmonic amplitudes generated by the MOSS modulation (fast component).

inclination angles $\gamma = 105^\circ$ and $\gamma = 75^\circ$. The rapid fringes are produced by the MOSS modulation at frequency Ω (see equation (15)). The slower modulation in fringe contrast and phase is generated by the electro-optic modulation of the second delay plate phase $\delta_2 \sin(\Omega_P t)$. The shift in the interferogram phase is manifested as a change in the ratio of fundamental and second harmonic components of the MOSS frequency, as the phase offset about which the interferogram is being modulated is advanced or retarded. More comprehensive experimental results will be presented elsewhere [23].

6. Imaging of relative emission line intensities

Similar ideas to those outlined above can be applied to the measurement of emission line intensity ratios—a powerful technique for estimating the relative abundances of isotopes [24], as well as other plasma parameters. For example, it has been established that the ratio of the emission intensities I_1 and I_2 of helium singlet and triplet transition radiation is a sensitive measure of the electron temperature [25,26]. Unfortunately, calculation of the ratio $\rho = I_1/I_2$ from independent light intensity measurements, can be noise prone, especially when the emission intensities are weak or the lines significantly overlap. Moreover, estimation of the ratio requires careful relative calibration of the sensitivities of the detection channels for each spectral line. When the spectral lines are very close, they can be difficult to resolve because of thermal broadening and other effects.

We have recently applied coherence-imaging techniques for sensitive and direct estimation of the ratio of H_β and D_β emission from resonantly rf heated plasmas in the H-1 heliac [27]. When the intensity ratio of a simple line pair changes, the spectral centre of mass of the line pair shifts, giving rise to both a phase shift and contrast change. By monitoring the coherence, the separate line-integrated component intensities can be recovered using just a single detector element per viewing sightline. This obviates the need for relative channel sensitivity calibration and opens the way for two-dimensional imaging of relative isotope abundances, electron temperatures or other physical parameters upon which the intensity ratio is dependent.

6.1. Measurement principle

For a pair of spectral lines, the total interferogram can be expressed as (see equation (11))

$$\begin{aligned} S &= I_1(1 + \zeta_1 \cos\phi_1) + I_2(1 + \zeta_2 \cos\phi_2) \\ &= I_0[1 + \zeta \cos(\phi_0 + \eta)] \end{aligned} \tag{45}$$

where

$$I_0 = I_1 + I_2 \tag{46}$$

$$I_0 \zeta \cos\eta = (I_1\zeta_1 + I_2\zeta_2)\cos\delta \tag{47}$$

$$I_0 \zeta \sin\eta = (I_1\zeta_1 - I_2\zeta_2)\sin\delta \tag{48}$$

and we have introduced the mean and difference phases $\phi_0 = (\phi_1 + \phi_2)/2$ and $\delta = (\phi_1 - \phi_2)/2$. When modulation is applied, the delay modulation term $\tilde{\phi}_1$ must of course be included in the interferometer phase. When the separation of the line pair is small, that is $\xi_P \equiv \Delta\lambda_P/\lambda_0 = \Delta\nu_P/\nu_0 \ll 1$, the difference phase is closely approximated by

$$\delta = \kappa\phi_0 \frac{\Delta\nu_P}{\nu_0} \equiv \hat{\phi}_0 \xi_P. \tag{49}$$

The difference phase δ can be calculated from the known birefringent phase shift ϕ_0 and the spectral line frequencies.

The total interferogram intensity I_0, phase $\phi_0 + \eta$ and contrast ζ are extracted numerically from the digitized MOSS light signals. Provided there is a known fixed relationship between the component contrasts ζ_1 and ζ_2, the three independent equations (46)–(48) then allow determination of the unknown intensities and the spectral line widths.

The choice of optimum optical delay difference δ is dictated by the ratio of the spectral line separation $\Delta\lambda_P = \lambda_2 - \lambda_1$ (H_β 486.133 nm and D_β 486.005 nm), to spectral line width (in our case, this is typically ~0.02 nm—see figure 12). For simplicity, assuming $\zeta_1 \approx \zeta_2 \equiv \zeta_0$, it can be seen that it is desirable to maximize the quantity $\zeta_0 \sin\delta$ in order to be most sensitive to the intensity difference expressed by equation (48). For a Gaussian spectral lineshape $\exp(-\sigma^2\xi^2/2)$ of normalized width σ, it is straightforward to show that the optimum delay difference δ (or equivalently, delay offset $\hat{\phi}_0$) is given by the solution to

$$\delta \tan\delta = \left(\frac{\xi_P}{\sigma}\right)^2. \tag{50}$$

When the separation ξ_P is large compared to the width σ this yields $\hat{\phi}_0 \to \pi/2$ corresponding to the first node of the interference beat pattern. When the width is large, the degradation of the spectral line contrast dominates and the optimum delay becomes $\hat{\phi}_0 \to 1/\sigma$, at which point the spectral line contrast is $1/e^2$. Figure 13 shows the variation of the optimum phase δ with the width to separation ratio σ/ξ_P together with the associated optimum sensitivity factor $\zeta_0 \sin\delta$.

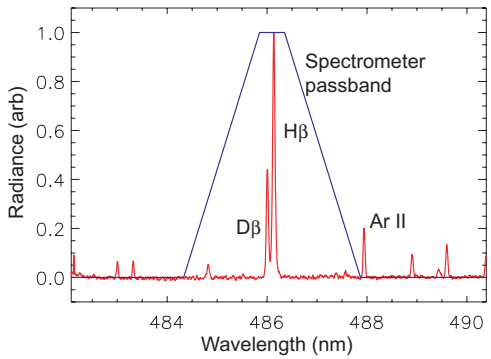

Figure 12. The H_β and D_β spectral lines in relation to the grating spectrometer pre-filter passband. There is some contamination by Ar II lines which is compensated in the analysis.

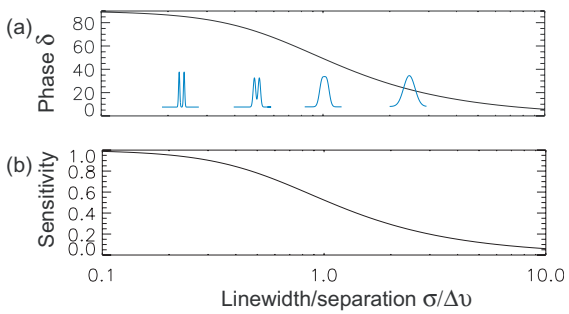

Figure 13. (*a*) Optimum difference phase δ versus ratio of spectral line width to separation σ/ξ_P and (*b*) the associated relative sensitivity factor $\zeta \sin\delta$ versus σ/ξ_P. The inset cartoons in (*a*) represent the variation of the line pair profile as the width/separation ratio increases. See text for discussion.

It is notable that reasonable sensitivity to the difference intensity persists up to $\sigma/\xi_P \lesssim 10$, allowing the relative abundance to be estimated without the need for profile-fitting.

6.2. H/D isotope relative abundance measurements in H-1

A recent improvement to the MOSS camera has been to replace the interference filter used for isolating the spectral region of interest with a high-throughput low-resolution grating spectrograph. The MOSS and imaging optics form an image of the plasma on the 1 mm wide entrance slit. This is subsequently re-imaged through the spectrograph onto a 16-element linear multi-anode photomultiplier tube array located in the spectrograph image plane. The best-fit trapezoidal instrument response used in these experiments is shown in figure 12. Though not as light-efficient as the interference filter, this arrangement offers much greater wavelength flexibility and background light rejection.

Based on the representative experimental spectrum shown in figure 12 and using equations (47) and (48), we have modelled the variation of the interferogram contrast and phase as a function of the ratio ρ of H to D atoms and mean waveplate delay ϕ_0 (see figure 14). The low-level irregularites in the contours are produced by contaminating lines within the spectral passband. For these experiments a lithium niobate birefringent plate of thickness 5 mm gives a calculated difference delay $\delta = 71^\circ$ and a mean delay $\phi_0/2\pi = 950$ waves leading to only minimal contrast degradation for the separate components ($\zeta_0 \sim 0.92$). The delay at which our measurements are made is indicated by the vertical line in figure 14. The calculated difference phase can be checked experimentally by using equations (47) and (48) in the case where either the hydrogen or deuterium intensities are negligible. The experimental value $\delta_{\text{expt}} = 70 \pm 5^\circ$ is found to be in good agreement with that calculated using equation (49) and the Sellmeier equations for lithium niobate (see, e.g. [28]).

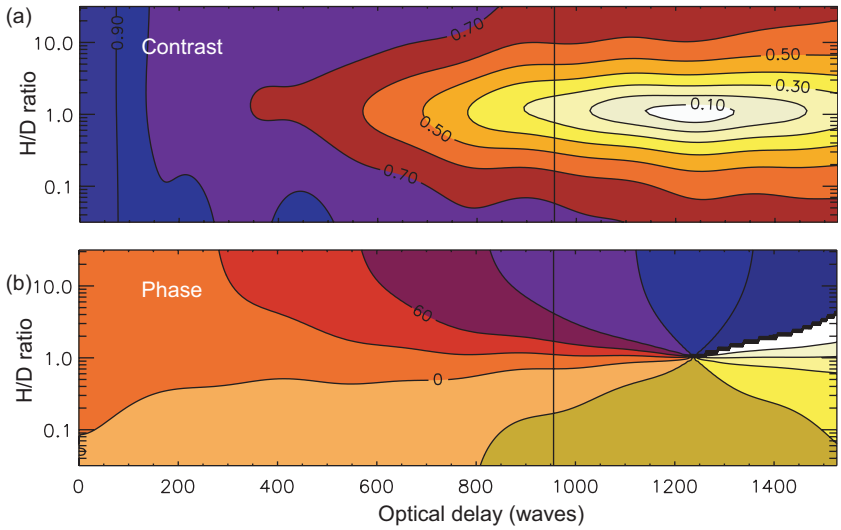

Figure 14. Calculated variation of interferogram contrast and phase as a function of crystal plate delay and H/D ratio. The phase varies as one or other of the spectral components dominates. The fringe contrast is a minimum when the intensities are equal (maximum effective spectral width). The vertical line indicates the crystal plate delay used in the experiments reported here. The low-level irregularities are due to the contaminating components and background passed by the spectrometer and shown in figure 12.

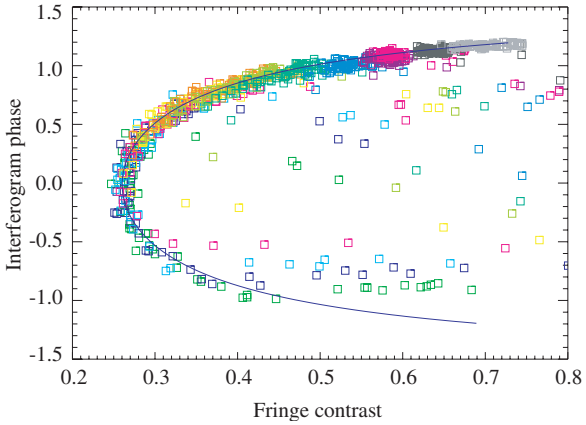

Figure 15. The model and observed variations of contrast and phase for H/D ratio measurements in H-1. The different symbol shades are for different initial H/D fill pressure ratios.

When the relative line intensities change, the interferogram contrast and phase are constrained by equations (46)–(48) to lie on the the curve

$$\frac{\zeta}{\zeta_2}\sin(\delta-\eta)+\frac{\zeta}{\zeta_1}\sin(\eta+\delta)=\sin 2\delta. \tag{51}$$

Figure 15 shows the calculated interferogram phase shift η versus fringe contrast ζ for a 5 mm thick delay plate. Superimposed are experimentally measured $\zeta - \eta$ traces for one of the camera channels. The different shades indicate distinct discharges covering a range of static fill mixtures of hydrogen and deuterium. Hydrogen rich discharges occupy the upper branch of the curve. Observe that the contrast is a minimum when the particle numbers are equal, and that the interferogram phase shifts as one or other of the species dominates. The close correspondence between model and measurement confirms that the instrument is properly measuring the light intensity ratios. Outlier points are due to errors in calculation of the phase and contrast when the light intensity is low.

Figures 16(*a*) and (*b*) show the temporal evolution of the emission intensity, and interferogram phase and contrast for the camera channel closest to the helical ring conductor (topmost in figure 3). The data were obtained for discharges in mixtures of H and D with relative pressures (*a*) (p_H : 0.02, p_D : 0.98) and (*b*) (p_H : 0.5, p_D : 0.5), keeping the total gas pressure constant at 7×10^{-6} Torr. The discharges were undertaken at a field strength of 0.5 T corresponding to the hydrogen ion cyclotron resonant frequency for 7 MHz rf excitation. The relative line-integrated atom number densities extracted from the emission intensity and spectral coherence are also shown. The delay to breakdown in discharge (*a*) is due to the inefficiency of the resonant minority heating scheme when the gas is hydrogen starved. Note, however, the gradual increase in H/D ratio signalled by the ramp in the interferometric phase and decrease in fringe contrast during the discharge evolution. This behaviour, which is most pronounced for this inner spatial channel, suggests a considerable release of hydrogen gas from the surface of the helical conductor during the plasma pulse. The effect is evident also for discharge (*b*) having equal H and D partial fill pressures.

The cross-section and pulse-averaged brightness ratios are shown as a function of relative fill pressure in figure 17. For comparison are overplotted the pulse-integrated brightness ratios obtained using a grating spectrometer (see figure 12) coupled to a fibre collecting radiation along a toroidal plasma chord. The agreement is satisfactory, while the data confirm

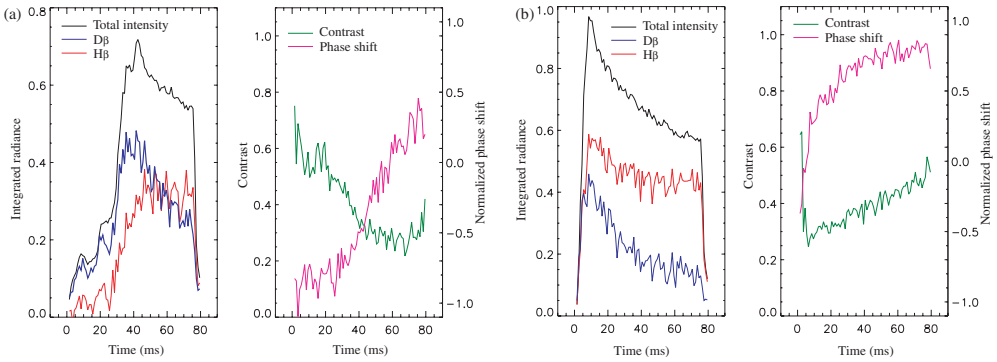

Figure 16. Time evolution of the total light intensity and its H_β and D_β components (left) derived from associated phase and contrast variations (right) for the camera channel viewing closest to the internal helical field winding. Relative static fill pressures are (*a*) $p_H : p_D = 0.02 : 0.98$ and (*b*) $p_H : p_D = 0.50 : 0.50$. In (*a*) it is clear that hydrogen released from the plasma facing components increases rapdily, equalling the deuterium brightness approximately 50 ms into the discharge where the fringe contrast is minimum.

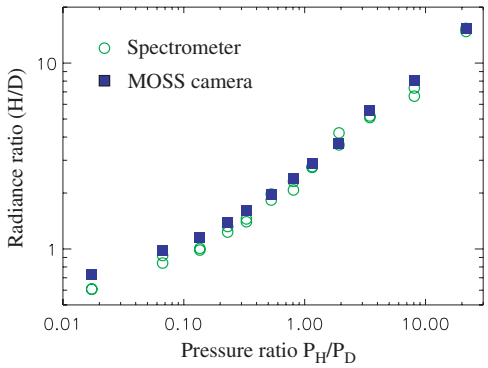

Figure 17. Comparison of the space and time averaged brightness ratio versus fill pressure ratio p_H/p_D for the MOSS imaging camera (■) and using the grating spectrometer (○). Minor discrepancies may be due to the fact that the grating spectrometer views the plasma along a toroidal chord while the camera data is from a poloidal cross-section. The data show disproportionately high emission from hydrogen most likely due to plasma-liberation of hydrogen from material surfaces.

that hydrogen liberated from in-vessel walls and components is contributing significantly to the plasma particle inventory. More detailed results from these studies, including spatial distributions and magnetic-configuration dependence will be presented elsewhere. As a result of these and other impurity radiation studies, new coil and tank heating systems are being installed to remove hydrogen and impurities trapped on the stainless-steel plasma-facing surfaces, while calibrated supersonic gas injection systems are being designed for targeted plasma fuelling.

7. Multiple delay spread-spectrum systems

As shown in section 4.1, a single delay camera will not provide sufficient information to characterize more complex lineshapes. The spread-spectrum optical Fourier transform (SOFT)

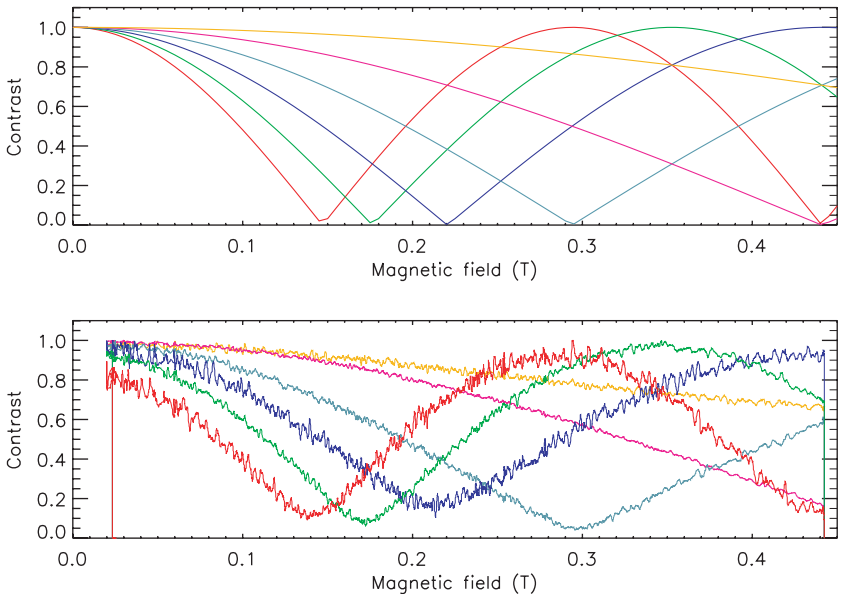

Figure 18. The Zeeman beat pattern monitored simultaneously at six independent interferometric delays using a 3-crystal plate SOFT system. The longer-delay measurements show a more rapid beating of the two components with increasing magnetic field.

spectrometer allows simultaneous measurements of the coherence of a narrowband spectral feature at a multiplicity of delays. SOFT is a generalization of the MOSS spectrometer that utilizes a number of birefringent electro-optic plates mutually aligned at 45° and placed between crossed or parallel polarizers. As its name suggests, the coherence information is now encoded across a series of harmonics of the common sinusoidal drive voltage applied to the electro-optic crystals [13]. The instrument is the coherence-analog of a slit spectrometer equipped with an image plane detector array. The SOFT, however, uses a single detector per spatial channel, the 'spectral' pixels are the harmonic carriers in the temporal frequency domain.

Results obtained using a three-crystal plate system (six independent delays) observing the Zeeman-split σ components of the Zn 468 nm line are shown in figure 18. The longer-delay measurements show a more rapid beating of the two components with increasing magnetic field. While there is reasonable agreement between our observations and low-field Zeeman-effect calculations, care must be taken to avoid unwanted etalon effects which are temperature and alignment sensitive. Further research is being undertaken to improve the accuracy and reliablility of these multi-component systems.

Acknowledgments

The authors wish to thank Boyd Blackwell for assistance with H-1 operations and helpful discussions, and Jeffrey Harris for continued positive support.

Appendix

With the magnetic field aligned along the z'-axis in the primed system (x', y', z') we take the transformation from the primed to the unprimed (laboratory) system to be given by the

rotation matrix

$$\boldsymbol{R}_{\theta,\psi} = \begin{bmatrix} \cos\theta & -\sin\theta\sin\psi & \sin\theta\cos\psi \\ 0 & \cos\psi & \sin\psi \\ -\sin\theta & -\cos\theta\sin\psi & \cos\theta\cos\psi \end{bmatrix} \tag{A1}$$

where the angles θ and ψ are defined in figure 7. In the primed system the Jones vectors for linear and circular polarized light are given by

$$\boldsymbol{E}'_{\sigma\pm} = \frac{1}{2}\begin{bmatrix} \pm\mathrm{i} \\ 1 \\ 0 \end{bmatrix} \qquad \boldsymbol{E}'_{\pi} = \frac{1}{\sqrt{2}}\begin{bmatrix} 0 \\ 0 \\ 1 \end{bmatrix} \tag{A2}$$

with relative intensities appropriate for the normal Zeeman triplet.

Transforming to the laboratory frame, and for observation along the z-axis, the component electric field vectors are given by

$$\boldsymbol{E}_{\sigma\pm} = \frac{1}{2}\begin{bmatrix} \pm\mathrm{i}\cos\theta - \sin\theta\sin\psi \\ \cos\psi \end{bmatrix} \qquad \boldsymbol{E}_{\pi} = \frac{1}{\sqrt{2}}\begin{bmatrix} \sin\theta\cos\psi \\ \sin\psi \end{bmatrix}. \tag{A3}$$

The components of the Stokes vector are defined in terms of the components of the electric field vector $[a_1 \exp(-\mathrm{i}\varphi), a_2]^{\mathrm{T}}$ as [4]

$$s_0 = a_1^2 + a_2^2 \tag{A4}$$
$$s_1 = a_1^2 - a_2^2 \tag{A5}$$
$$s_2 = 2a_1a_2\cos\varphi \tag{A6}$$
$$s_3 = 2a_1a_2\sin\varphi \tag{A7}$$

with normalization

$$I_0 \equiv s_0^2 = s_1^2 + s_2^2 + s_3^2. \tag{A8}$$

Noting the relations between the angles in figure 7

$$\cos\theta\cos\psi = \cos\gamma \tag{A9}$$
$$\sin\psi = \sin\gamma\sin\beta \tag{A10}$$
$$\sin\theta\cos\psi = \sin\gamma\cos\beta \tag{A11}$$

the Stokes vectors for the π and σ components can be expressed in terms of the angles β and γ as

$$\boldsymbol{s}_{\pi} = \tfrac{1}{2}(\sin^2\gamma\cos 2\beta, \sin^2\gamma\sin 2\beta, 0), \tag{A12}$$
$$\boldsymbol{s}_{\sigma\pm} = \tfrac{1}{4}(-\sin^2\gamma\cos 2\beta, -\sin^2\gamma\sin 2\beta, \mp 2\cos\gamma) \tag{A13}$$

with normalization

$$I_{\pi}(\gamma) = \frac{I_0}{2}\sin^2\gamma \tag{A14}$$
$$I_{\pm\sigma}(\gamma) = \frac{I_0}{4}(1+\cos^2\gamma) \tag{A15}$$

where I_0 is the spectrally integrated irradiance, or brightness of the multiplet.

References

[1] Jacquinot P 1954 *J. Opt. Soc. Am.* **44** 761
[2] Howard J, Michael C, Glass F and Cheetham A 2001 *Rev. Sci. Instrum.* **72** 888
[3] Howard J 2002 *Appl. Opt.* **41** 197
[4] Born M and Wolf E 1980 *Principles of Optics* (Oxford: Pergamon)
[5] Goodman J 1985 *Statistical Optics* (New York: Wiley)
[6] Weiss R S and Gaylord T K 1985 *Appl. Phys.* A **37** 191
[7] Steel W 1967 *Interferometry* (Cambridge: Cambridge University Press)
[8] Biazzo M R 1971 *Appl. Opt.* **10** 1016
[9] Howard J *et al* 2003 *Rev. Sci. Instrum.* **74** 2060–63
[10] Michael C, Howard J and Blackwell B D 2001 *Rev. Sci. Instrum.* **72** 1034
[11] Rees D and Greenaway A 1983 *Appl. Opt.* **22** 1078
[12] Bell R *et al* 1999 *Rev. Sci. Instrum.* **70** 821
[13] Howard J and Michael C 2003 in preparation
[14] Collis S *et al* 2003 *Rev. Sci. Instrum.* **74** 1629–32
[15] Michael C and Howard J in preparation
[16] Howard J 1999 *Plasma Phys. Control. Fusion* **41** 271
[17] Feldman U *et al* 1984 *J. Appl. Phys.* **56** 2512
[18] Wroblewski D, Huang L K and Moos H W 1988 *Rev. Sci. Instrum.* **59** 2341
[19] Kuramoto H *et al* 1997 *Fusion Eng. Design* **34–35** 285
[20] Thomas D *et al* 2001 *Rev. Sci. Instrum.* **72** 1023
[21] Candler C 1964 *Atomic Spectra* (London: Hilger and Watts)
[22] Howard J 1996 *Plasma Phys. Control. Fusion* **38** 489
[23] Howard J and Danielsson A 2003 *Appl. Spectrosc.* in preparation
[24] Hillis D L *et al* 1999 *Rev. Sci. Instrum.* **70** 359
[25] Field A R, Carolan P G, Conway N J and O'Mullane M G 1999 *Rev. Sci. Instrum.* **70** 355
[26] Carraro L *et al* 2000 *Plasma Phys. Control. Fusion* **42** 1
[27] Howard J, Blackwell B and Michael C 2003 in preparation
[28] http://www.crystaltechnology.com/productdata.html